ARL-TR-9979 • Sep 2024

Computational Investigation of Control Effectors on a Generic High-Speed Vehicle

by Justin Paul, James DeSpirito, and Jubaraj Sahu

ARL-TR-9979 ● SEP 2024

Computational Investigation of Control Effectors on a Generic High-Speed Vehicle

Justin Paul and James DeSpirito
DEVCOM Army Research Laboratory

Jubaraj Sahu
SURVICE Engineering Company

REPORT DOCUMENTATION PAGE

1. REPORT DATE	2. REPORT TYPE	3. DATES COVERED	
		START DATE	END DATE
September 2024	Technical Report	31 August 2022	31 May 2024

4. TITLE AND SUBTITLE
Computational Investigation of Control Effectors on a Generic High-Speed Vehicle

5a. CONTRACT NUMBER	5b. GRANT NUMBER	5c. PROGRAM ELEMENT NUMBER
5d. PROJECT NUMBER	**5e. TASK NUMBER**	**5f. WORK UNIT NUMBER**

6. AUTHOR(S)
Justin Paul, James DeSpirito, and Jubaraj Sahu

7. PERFORMING ORGANIZATION NAME(S) AND ADDRESS(ES)	8. PERFORMING ORGANIZATION REPORT NUMBER
DEVCOM Army Research Laboratory ATTN: FCDD-RLA-WD Aberdeen Proving Ground, MD 21005	ARL-TR-9979

9. SPONSORING/MONITORING AGENCY NAME(S) AND ADDRESS(ES)	10. SPONSOR/MONITOR'S ACRONYM(S)	11. SPONSOR/MONITOR'S REPORT NUMBER(S)

12. DISTRIBUTION/AVAILABILITY STATEMENT
DISTRIBUTION STATEMENT A. Approved for public release: distribution unlimited.

13. SUPPLEMENTARY NOTES
ORCID: Justin Paul, 0000-0003-4133-7585

14. ABSTRACT
In this investigation, several configurations of a generic high-speed test vehicle were simulated and analyzed with control effectors in the shape of rectangular prisms. The performance of the control effectors was then determined in the context of an equivalent tail-flap control to estimate the control authority the control effectors offered. The comparison indicates that the control effectors generate appreciable control authority. Additionally, the effectiveness and performance of the control effectors were assessed at different axial locations (three configurations) and through a sweep of angle of attack (two configurations). Three of the six configurations investigated were found as potentially viable for pitch and roll maneuvers.

15. SUBJECT TERMS
Weapons Sciences, supersonic flow, ballistics, computational fluid dynamics, aerodynamic control, computational fluid dynamics, Euler CFD code

16. SECURITY CLASSIFICATION OF:			17. LIMITATION OF ABSTRACT	18. NUMBER OF PAGES
a. REPORT	b. ABSTRACT	C. THIS PAGE		
UNCLASSIFIED	UNCLASSIFIED	UNCLASSIFIED	UU	39

19a. NAME OF RESPONSIBLE PERSON	19b. PHONE NUMBER *(Include area code)*
Justin Paul	(410) 306-0797

STANDARD FORM 298 (REV. 5/2020)
Prescribed by ANSI Std. Z39.18

Contents

List of Figures

List of Tables

1. Introduction

In the 2000s, efforts were initiated to better understand how "pin-based" actuators could be used to guide supersonic projectiles.[1–8] These control effectors were investigated in a variety of ways such as comparing configurations for better cross-range metrics and analyzing mechanical feasibility while attempting to transform the pressure distribution over stabilizing control surfaces.[1–3,5,7] Trajectory simulations and spark range experimentation were also conducted to evaluate the value of the technology.[4,6] Work continued beyond 2010, analyzing the effectiveness of similar "micro-flap" control effectors using computational fluid dynamics (CFD) simulations and coupled CFD/rigid-body dynamics flyout trajectory simulations.[9–15]

The approach of this investigation is to compare similar "pin-type" control effector aerodynamic performance to the performance offered by tail-flap control, which was recently characterized on this same generic test vehicle.[16–23] The method of the comparison was to calculate an "equivalent" flap deflection angle corresponding to a given control effector configuration. The benefit of such novel control effectors would be the possibility of enhanced control authority and more compact packaging. The terms "pin" and "control effector" are used interchangeably throughout.

2. Geometry Definition

The test configuration, Fig. 1, was a generic, axisymmetric ogive-cylinder body with four high-sweep, low-aspect ratio clipped-delta fins. It featured a 3-diameter-long, blunt von Kármán ogive nose with a 0.1-diameter nose radius. The model had a slenderness ratio of 10. The root fin chord of the fins was 6 diameters long, the tip fin chord was 2.2 diameters long, and the fin span was 1.935 diameters. The diameter of the body was 0.105 m. Control is provided using movable trailing edge flaps on each of the four fins to provide sufficient control authority to execute desired maneuvers.[24]

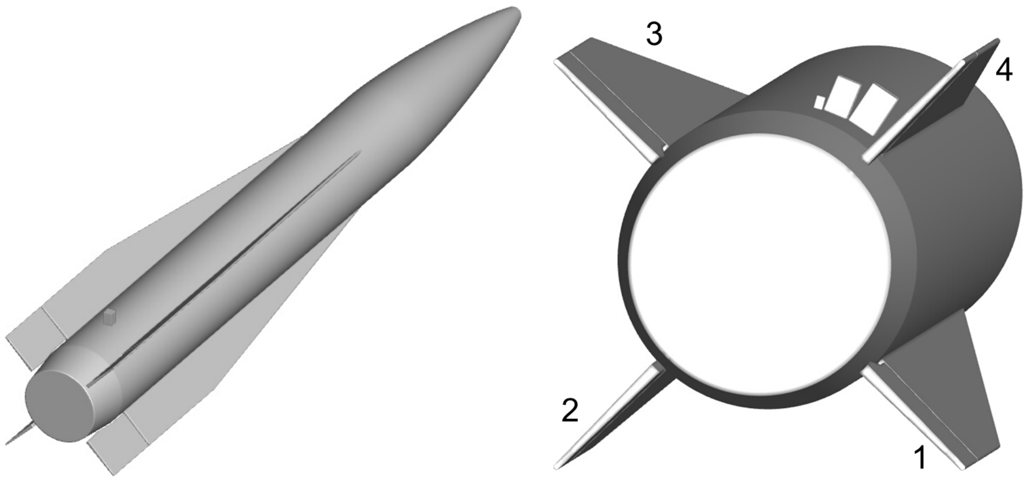

Fig. 1 Flight vehicle with control effector centered on top of vehicle (left) and all three control effector sizes placed next to each other (right). Numbers on the right-hand image represent each fin number.

In this investigation, the geometry was slightly modified by introducing the presence of the control effectors approximately 1.1 cal. from the base. The basic idea behind the use of these control effectors is that they would be deployed in various configurations to provide pitch, yaw, and/or roll control to maneuver as desired. When deployed, they alter the pressure distribution on the body and fins (depending on location) and provide a force that generates a pitch or roll moment. The control effectors are simplistic in the sense they are rectangular prisms with equal width and depth. In this investigation three different control effectors of various heights and widths were all analyzed with the same aspect ratio of 1.5. Figure 1 shows an illustration of the flight body with control effectors present. The image on the right side of Fig. 1 is not an actual configuration that was analyzed but simply an illustration of the three control effectors that were analyzed to indicate their relative size in comparison to each other. The pin sizes are listed in Table 1.

Table 1 Pin sizes

Dimension	Pin size 1 (mm)	Pin size 2 (mm)	Pin size 3 (mm)
Width/depth	3.00	10.50	8.80
Height	4.50	15.75	13.20

A description of the control effector configurations simulated and analyzed in this investigation is detailed in Table 2, where the images show a front view of the projectile. The maneuver control "positive roll" in Table 2 is defined as counterclockwise in this front view, and a "positive pitch" is nose up. The nomenclature CEMXX uses "X" as a placeholder for numerically designating the size of the pin (the first X) and configuration number designating the orientation of the pin(s) (the second X). All six configurations were simulated for all three control effector sizes excluding CEM18, the smallest control effector size. The single control effector configurations (CEMX3, CEMX6) are primarily to provide a baseline effect, and deployment of multiple control effectors in orientations similar to those in the table is the expected practical use for maneuver.

Table 2 Description of control effector configurations

Name	Description	Maneuver control	Images
CEMX3	Single control effector located on top of the projectile in the pitch plane	Pitch up	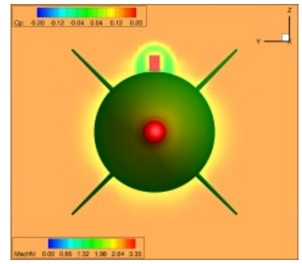
CEMX6	Single control effector located on top of the projectile near fin 4	Positive roll with pitch (coning)	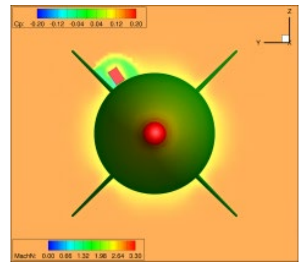
CEMX7	Two control effectors located on top of the projectile near fins 3 and 4	Pitch up	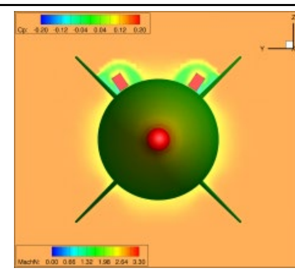
CEMX8	Two control effectors located on top of the projectile near fins 3 and 4 and two control effectors located on the sides of the projectile near fins 1 and 2	Pitch up	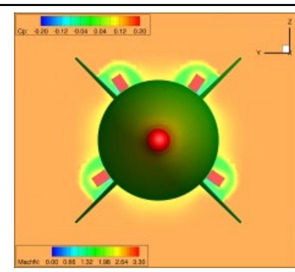
CEMX10	Four control effectors located on the same side of each fin	Postive roll	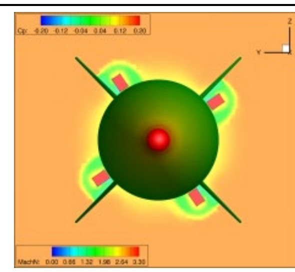
CEMX11	Two control effectors with one located near opposite fins	Positive roll	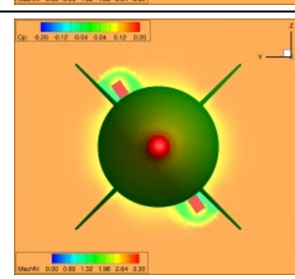

Additionally, this investigation includes an analysis of how the axial location of the control effectors impacts the pressure distribution generated by the control effectors. Both the change in the pressure distribution and the location of the pressure distribution change the aerodynamic performance of the control effectors. The different axial locations are illustrated in Figs. 2 and 3. Figure 2 shows the three axial locations and the center of gravity, $x_{c.g.}$, location referenced from the base of the vehicle. Figure 3 shows the CEMX3, CEMX7, and CEMX10 control effector configurations on the computational model at the three axial locations (left) and flow Mach number and surface pressure coefficient, C_p, contours (right). These three configurations were used in the analysis of the aerodynamic performance. The medium-sized control effector (CEM3X) was used in all configurations comparing the aerodynamic performance at different axial locations.

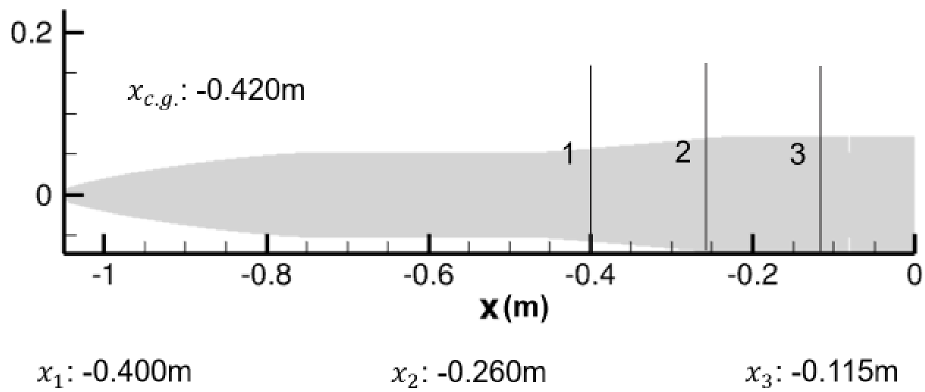

Fig. 2 Designation of axial locations along body

(a)

(b)

(c)

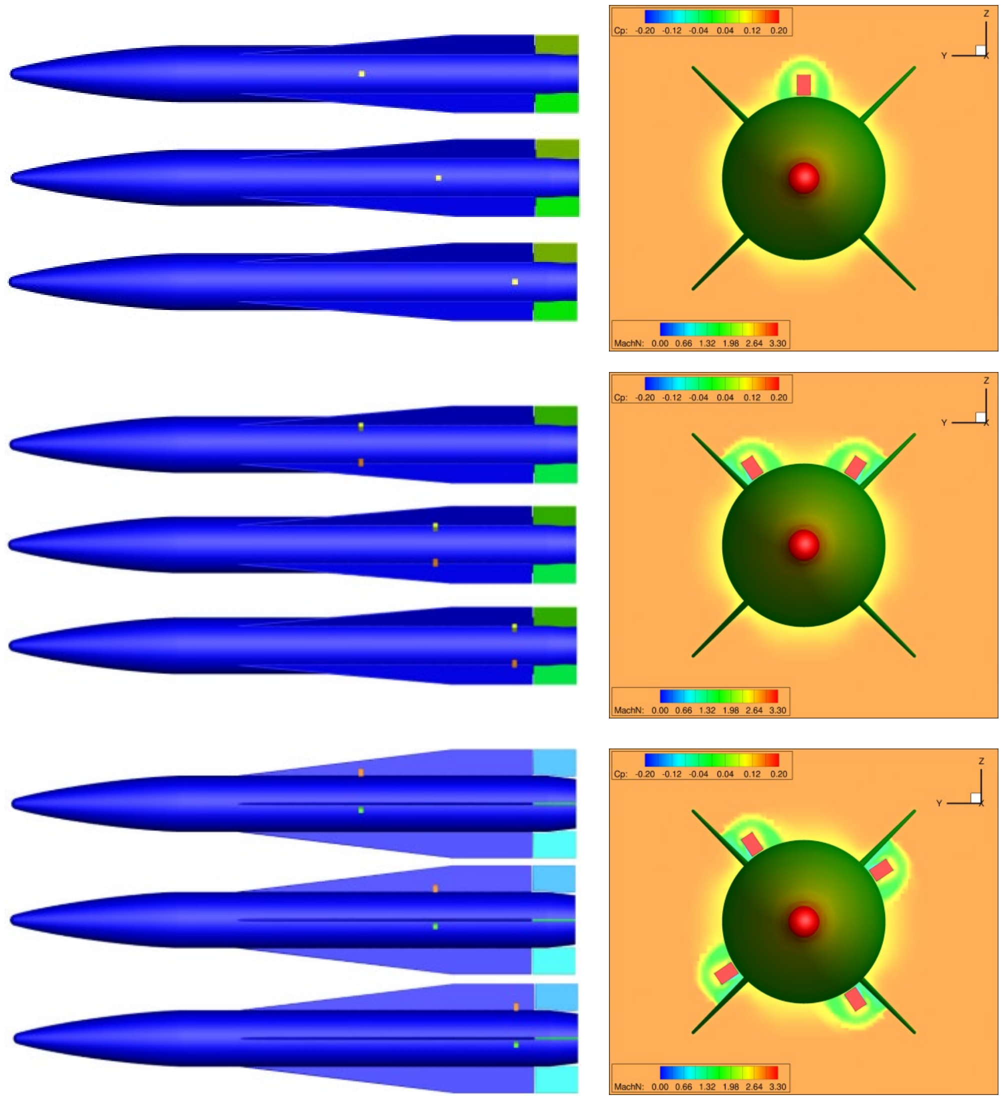

Fig. 3 Visualization of the three configurations featured in the analysis of axial locations. The first column depicts the configurations as viewed from the top (a, b) and in the top port fin span direction (c) while the second column clarifies what configuration is being analyzed.

3. Methodologies

Euler (inviscid) CFD was used to generate aerodynamic coefficient data, which was then interpolated with polynomial regression to create functions for plotting aerodynamic coefficients against flap deflection data in the context of the aerodynamic database.[18,20] The rationale of interpolating flap deflection data is to calculate an "equivalent" flap deflection angle based on the aerodynamic performance of a given control effector configuration. This enabled the comparison of aerodynamic performance of pin-type control effectors to tail-flap control.

3.1 Euler CFD Software: Cart3D

The data was generated from simulations using a software package called Cart3D developed by the National Aeronautics and Space Administration (NASA). NASA's Cart3D is an inviscid CFD package for aerodynamic design and analysis.[25] Cart3D provides utility for surface modeling and intersection, mesh generation, flow simulation, and postprocessing. The mesh generation software with the Cart3D package produces Cartesian meshes for arbitrarily complex, watertight geometries. The mesh generation process automatically increases the fidelity of the domain near small features and curvature present in the geometry to better resolve flow features near the surface. The Cart3D software suite also offers adjoint-based adaptive mesh refinement,[26] but only prescribed mesh refinement levels were used in this study.

The meshes generated for the simulations numbered approximately 1.3 million cells. This was the result of using 13 levels of refinement in a Cartesian computational domain with an inscribed sphere of 7 body lengths. An example of one of the meshes is shown in Fig. 4. Aerodynamic coefficients for a given flight condition (i.e., Mach number and aerodynamic angles) are computed in several minutes by the flow solver "flowCart".[27] For all simulations, the geometry was oriented in the x configuration in the mesh, as shown in the right image of Fig. 4. In this investigation, all simulations were executed at the flight condition of Mach 3. Initial screening of control effector type and orientation was performed at zero incidence angle, $\alpha = 0°$. Two configurations were then investigated at incidence angles $-15° \leq \alpha \leq 15°$.

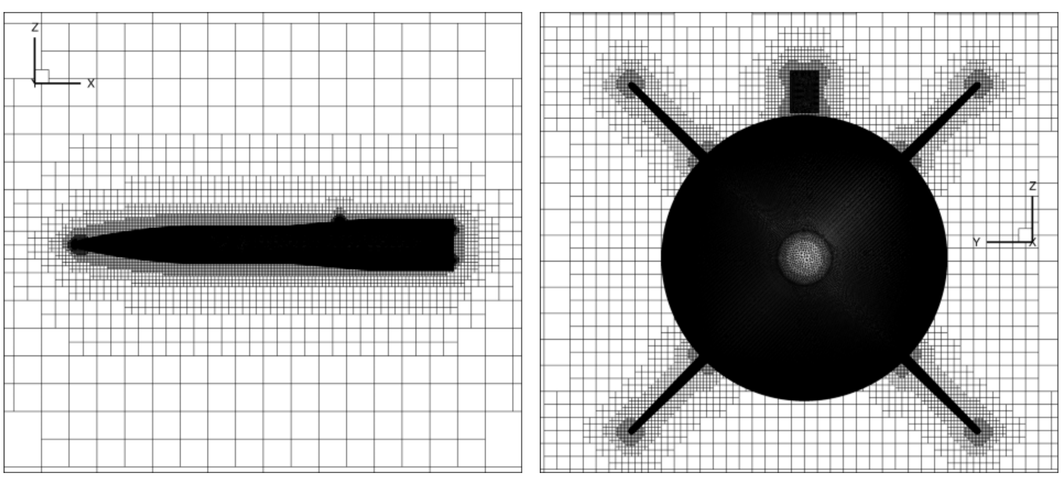

Fig. 4 Longitudinal (left) and axial (right) cut planes of computational mesh of the flight vehicle with a control effector on top

3.2 Polynomial Regression of Tail Flap Deflection Data

The aerodynamic database for this vehicle[19–21] includes flap deflection data for tail-flap control. An illustration of how the flaps deflect and the numbering system of the flaps are shown in Fig. 5. For this investigation, an existing aerodynamic model with flap control was used to obtain discrete aerodynamic performance metrics (C_m, C_N, C_l) at Mach 3 and $\alpha = 0°$ with all four flaps deflected between $-10° \leq \delta \leq 10°$. The pin control effector configuration performance was compared to flap-control maneuver control where all four flaps were deflected in either a pitch or roll maneuver, as appropriate, with the vehicle in the x flight orientation.

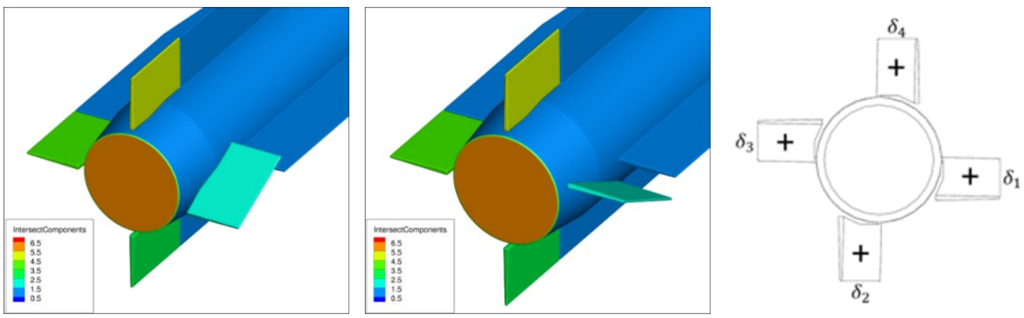

Fig. 5 Positive flap deflection, δ = 25° (left), negative flap deflection, δ = –25° (middle), and flap numbering system (right) (only flap 1 shown deflected)

The flap deflection data, shown in Fig. 6, was then fit with polynomial regression to obtain functions that represent a continuum of the flap performance between $-10° \leq \delta \leq 10°$. This investigation only considered the magnitude of "equivalent" flap deflection the control effectors offered. Since the magnitude of the flap-control load data is symmetric with flap deflection angle, only positive deflection angle is considered. In addition, the absolute value of the coefficient was used since all pin configurations give positive control loads. This transformation is shown in the lower section of Fig. 6. The aerodynamic performance of the vehicle with each control effector configuration was used to calculate a corresponding flap deflection angle using polynomial regression. This established a comparison between the pin control effector technology and the more well-established tail-flap control mechanism.

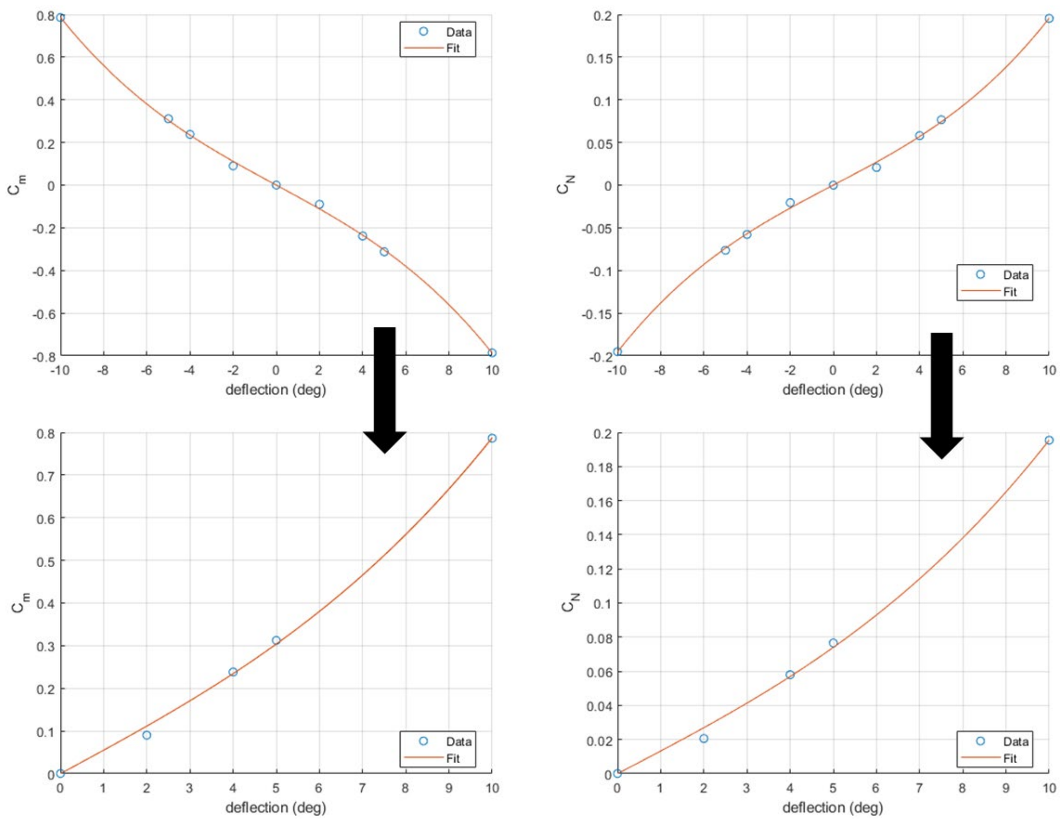

Fig. 6 Vehicle pitching moment (left) and normal force (right) coefficient variation with flap deflection over full flap deflection range (upper) and transformed to positive flap deflection only (lower)

4. Results

The results of this investigation are separated into four subsections. Section 4.1 presents the control effector configurations that were investigated and how the projectile surface pressure distribution and the flow field in immediate proximity to the control effector were affected. Section 4.2 presents the control effector aerodynamic performance obtained from the Cart3D simulations compared to the vehicle aerodynamic model with flap deflection data. Section 4.3 presents comparisons of different axial stations for chosen control effector configurations. Section 4.4 presents the aerodynamic performance of two control effector configurations as functions of incidence angle. The aerodynamic performance data plotted in Sections 4.2, 4.3, and 4.4 is tabulated in the Appendix.

4.1 Simulation Contours of Mach Number and Surface Pressure Coefficient

In this investigation, six different configurations of control effectors on the flight vehicle were analyzed. Among the six configurations investigated, three configurations were selected that were thought likely to have the best performance for pitch and roll maneuvers, as determined by the largest control pitching and rolling moments, respectively. All three control effector sizes for the control effector configuration identified for a pitch maneuver, CEMX7, are shown in Fig. 7. The sizes of the control effectors are shown as smallest on the left, largest in the middle, and medium on the right. The larger control effectors have a much more pronounced effect on the surface pressure distribution than the smallest control effector size (left column). The smallest control effector size appears to show little to no interaction between the two control effectors while the two larger control effector sizes are showing a shock intersection slightly aft of the control effectors' axial station. This observation indicates the potential for designing control effector configurations that could be arrays of control effectors with synergistic effects based on shock–shock interaction, as was investigated previously.[9–11] The larger control effectors also show larger high-pressure distribution on the fins, which augments the control loading.

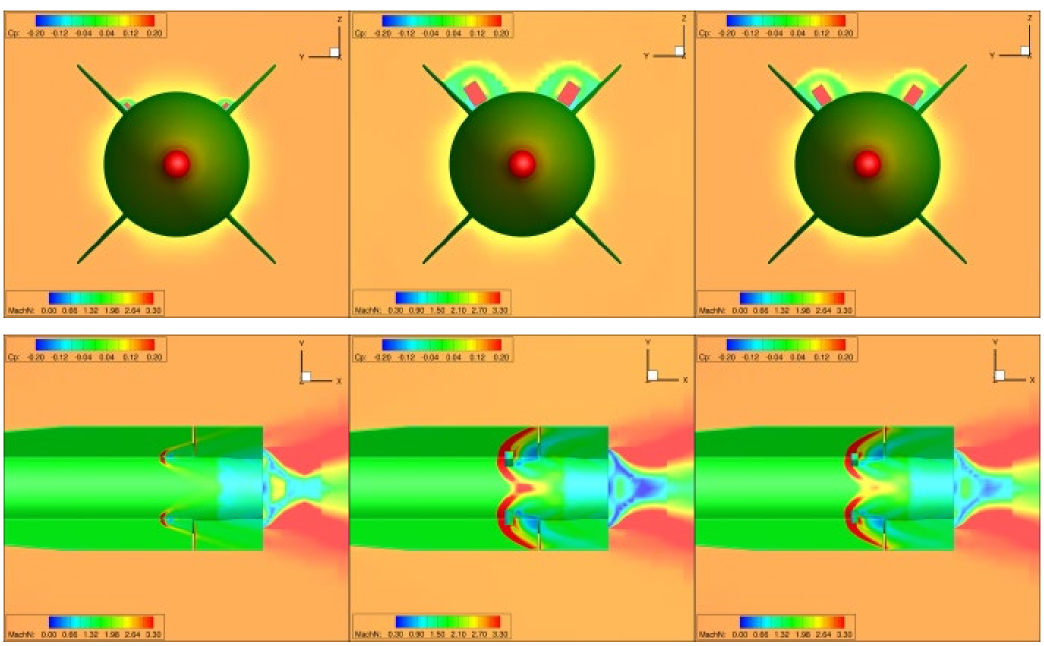

Fig. 7 Contours of Mach number and surface pressure coefficient for CEM17 (left), CEM27 (middle), and CEM37 (right), showing the front (first row) and the top view of the projectile (second row) at Mach 3 and $\alpha = 0°$

For a roll maneuver, two potential configurations were identified. All three control effector sizes for both roll maneuver configurations, CEMX10 and CEMX11, are shown in Figs. 8 and 9, respectively. The isolation of the effects generated by the control effectors is also applicable to both configurations for roll maneuver, which is because each control effector appears to have no interaction with any other control effector. In other words, the roll moment effects are expected to be linear—i.e., the C_l generated by configuration CEMX10 should be double the C_l generated by configuration CEMX11, which is discussed later. These two configurations can then be used to control the amount of roll control desired to impart to the vehicle while not imparting a transverse load on the vehicle. There is also a region of low pressure behind the control effectors in Figs. 7–9. The significance of this observation is that the low-pressure region forming behind the control effector works against the high-pressure region the control effector generates in front, thus decreasing the effectiveness of the control effector. This observation was also made in previous investigations, and attempts were made to mitigate it by moving the control effector as far aft as possible.[6] By moving the control effector aft, the low-pressure region might be off the body, and this decrease in performance can be mitigated.

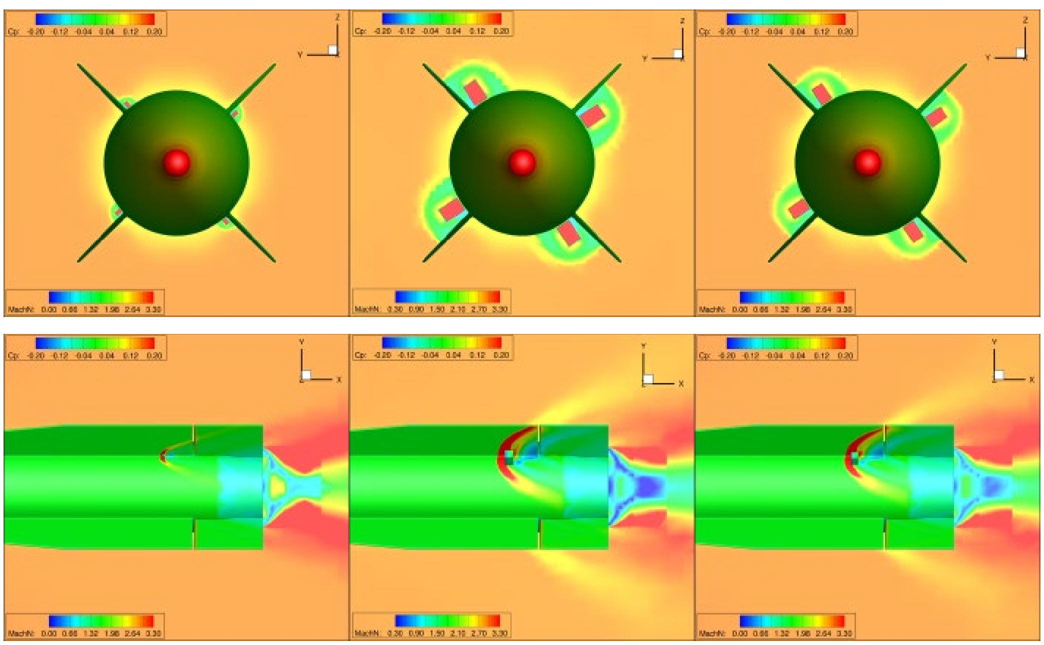

Fig. 8 Contours of Mach number and surface pressure coefficient for CEM110 (left), CEM210 (middle), and CEM310 (right), showing the front (first row) and the top view of the projectile (second row) at Mach 3 and $\alpha = 0°$

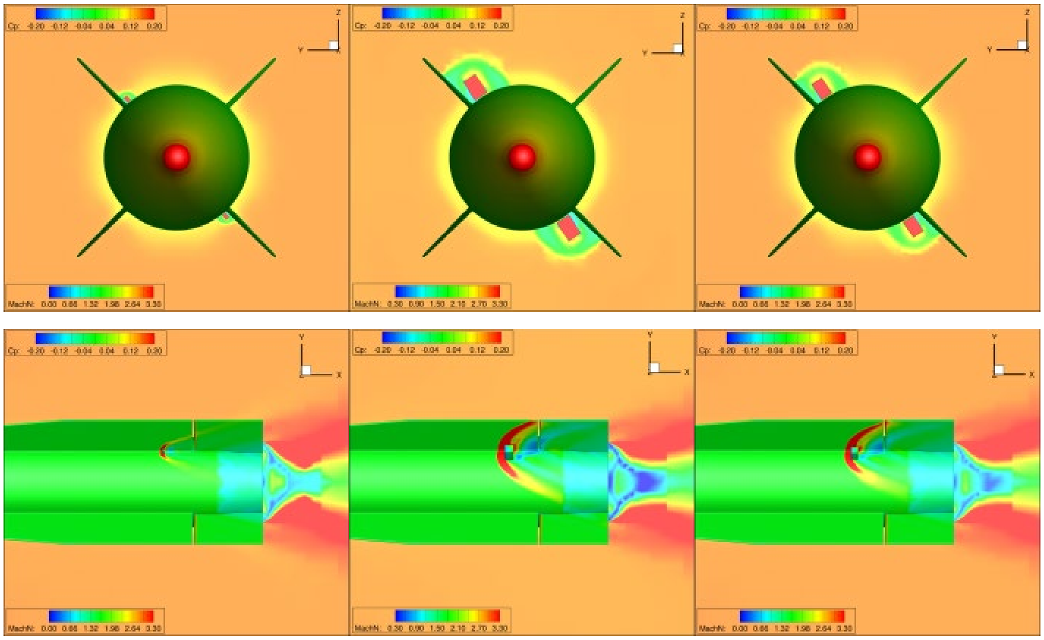

Fig. 9 Contours of Mach number and surface pressure coefficient for CEM111 (left), CEM211 (middle), and CEM311 (right), showing the front (first row) and the top view of the projectile (second row) at Mach 3 and $\alpha = 0°$

The other three configurations investigated are shown here in Fig. 10. Configuration CEMX3 was the first configuration simulated to determine the surface pressure that forms on the projectile from an isolated control effector and to help form a better idea of sizing the control effectors. Configuration CEMX6 was only simulated to isolate the roll moment generated from a single control effector. Since it also generates a transverse (pitching) moment, in general, it is not an optimum configuration. Finally, configuration CEMX8 was investigated to compare against configuration CEMX7. As will be shown in Section 4.2, the pressure distribution on the body due to the lower set of control effectors counteracts the desired maneuver control generated from the pressure distributions of the upper control effectors and the pressure distributions of the lower control effectors on the lower fins. Therefore, configuration CEMX8 generates only slightly more control moment than configuration CEMX7.

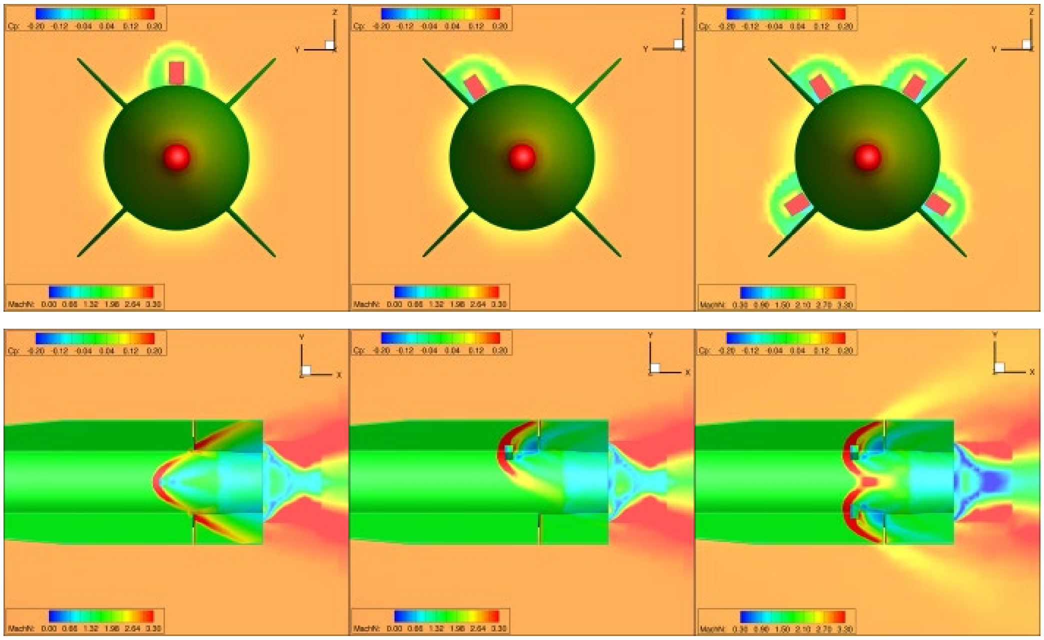

Fig. 10 Contours of Mach number and surface pressure coefficient for CEM23 (top), CEM26 (middle), and CEM28 (bottom) at Mach 3 and $\alpha = 0°$

4.2 Comparison of Aerodynamic Coefficients to Flap Deflection Data

The aerodynamic coefficients for the control effector configuration are compared in Figs. 11–15. The projectiles C_N and C_m for all three control effector sizes (when available) are plotted in each of the figures and can be compared against each other directly. The C_l is shown in Fig. 13 for both roll maneuver configurations CEMX10 and CEMX11 and in Fig. 15 for CEMX6, which induces both C_m and C_l.

The first observation about the aerodynamic performance of the control effector configurations is that the two larger control effector sizes do in fact generate appreciable aerodynamic control authority compared to the tail-flap control mechanism, greater than 4° and 3° for C_N and C_m, respectively, for CEMX7 (Fig. 11). Only the small control effector size has questionable control authority, which can be assessed using additional analysis and, potentially, trajectory simulations for a specified mission context. Additionally, as previously stated, configuration CEMX8 (Fig. 12) is not a significant improvement over CEMX7. While the increase in C_N is appreciable, the increase in C_m is only slightly more than that in configuration CEMX7 due the effect described in Section 4.1. The final noteworthy observation (Fig. 13) is that C_l generated by configuration CEMX10 is nearly linear, approximately double the C_l generated by CEMX11. This is useful in practice as it allows more roll control range by using either 2 or 4 control effector deployments. Configuration CEMX3 (Fig. 14) shows lower, but still significant maneuver control compared to CEMX7 (Fig. 11), indicating it as another viable configuration for pitch control. Configuration CEMX6 (Fig. 15) is not practical, as it produces small effective roll control while having the propensity to induce a coning motion of the projectile, as indicated by the significant C_n and C_m values.

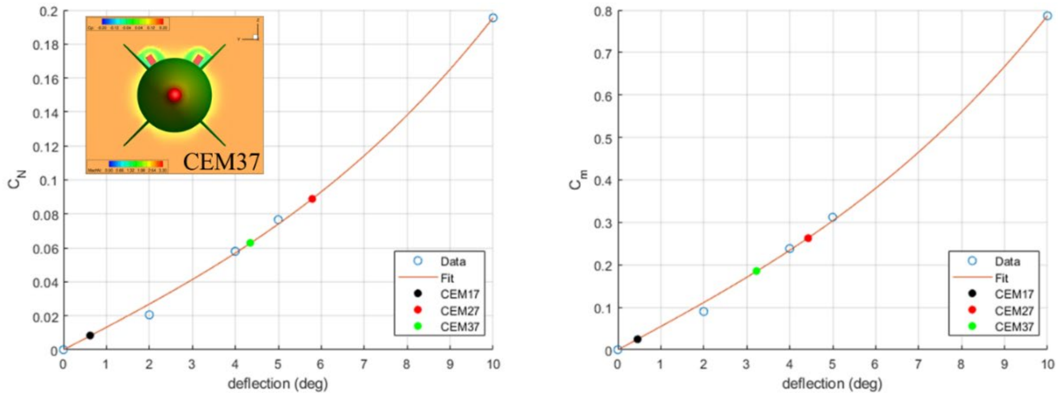

Fig. 11 C_N (left) and C_m (right) interpolated flap deflection data for CEM17, CEM27, and CEM37

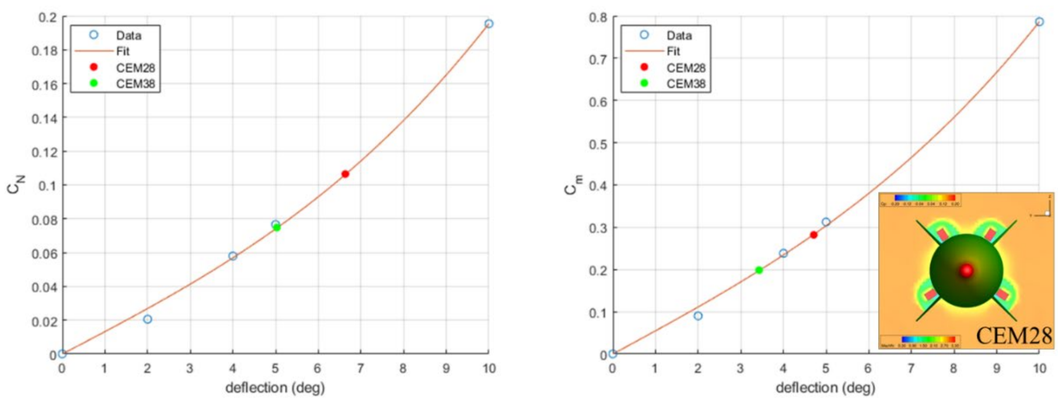

Fig. 12 C_N (left) and C_m (right) interpolated flap deflection data for CEM28 and CEM38

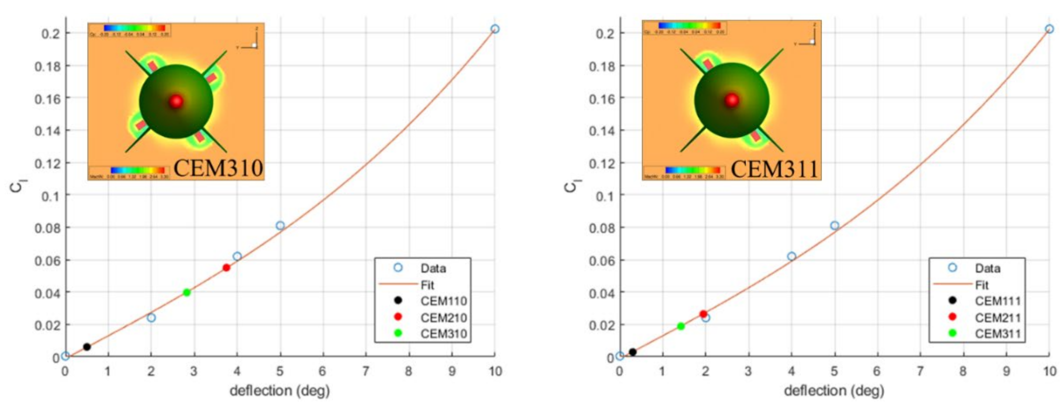

Fig. 13 C_l interpolated flap deflection data for CEM110 (left), CEM210 (left), CEM310 (left), and CEM111 (right), CEM211 (right), CEM311 (right)

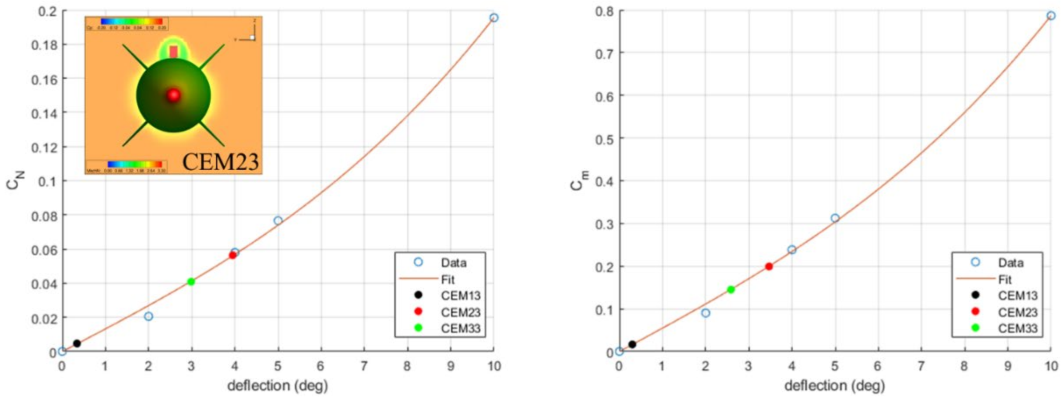

Fig. 14 C_N **(left) and** C_m **(right) interpolated flap deflection data for CEM13, CEM23, and CEM33**

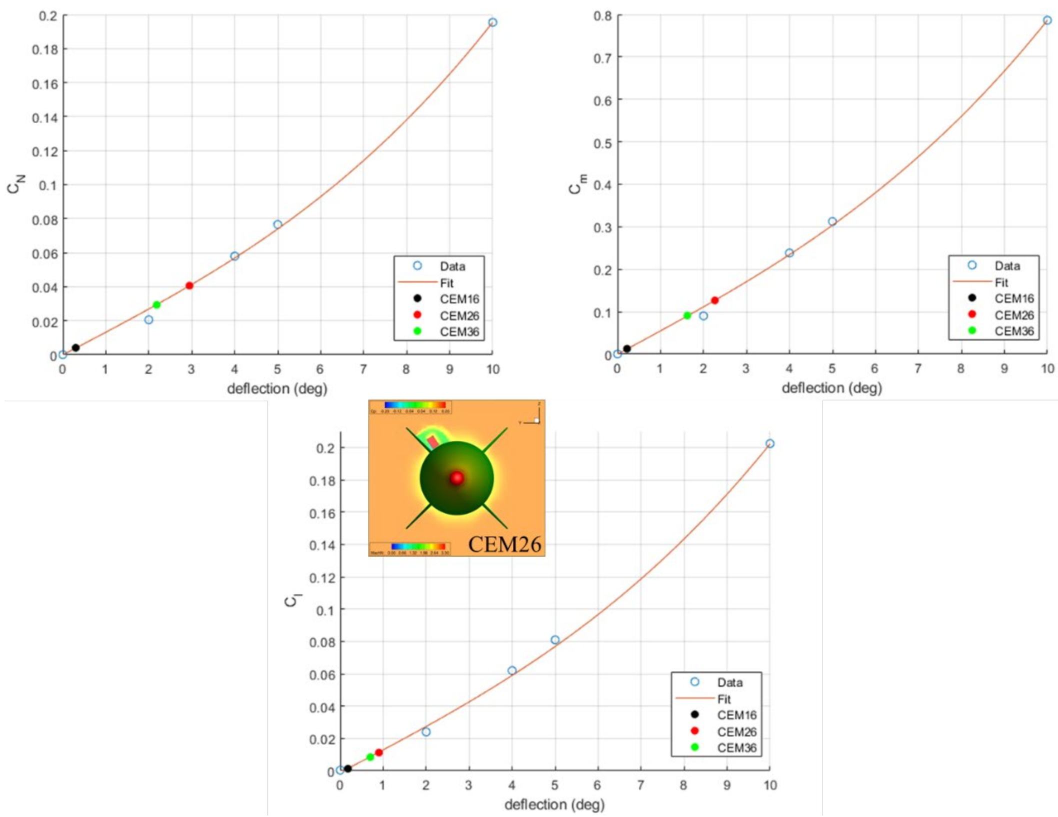

Fig. 15 C_N **(top left),** C_m **(top right), and** C_l **(bottom) interpolated flap deflection data for CEM16, CEM26, and CEM36**

4.3 Comparing Axial Control Effector Stations

Three different axial control effector stations (Fig. 2) were investigated to calculate and compare the aerodynamic coefficients that characterize aerodynamic performance (C_m, C_N, C_l). The results for C_N and C_m for two configurations for pitch control, CEM33 and CEM37, comparing different axial locations are shown in Fig. 16. In Fig. 16, the top two plots compare C_N and C_m directly. The plot of C_N shows the significant reduction in normal force as the control effector is moved away from the flow constraining effect of the fins (Figs. 2 and 3) and the benefit of locating them within the fin region. For example, if no fins were present, the normal force due to the control effector should be constant with axial location when the vehicle is at zero incidence. The lower plot in Fig. 16 requires additional explanation. Since the pitch moment at each axial location varies linearly with distance from the moment reference point (projectile center of gravity, $x_{c.g.}$) and the normal force at each location is significantly different, the pitch moment for configuration CEM37 was plotted two additional ways to help distinguish these effects. The blue curve is the predicted C_m at each axial location. The red curve in the bottom plot is calculated using the C_N at the third location ($x_3 = -0.115$ m) with the corresponding moment arm at the two other locations. This illustrates the obvious reduction in pitch control as the control effector is closer to the projectile center of gravity (smaller moment arm). The green curve is calculated using the C_N at each of the three locations with the moment arm corresponding to the third location ($x_3 = -0.115$ m), which should isolate the effect of the change in C_N with axial location. The $C_m \approx 0.05$ at the forward location corresponds to a flap deflection of approximately 1° (solid line in Fig. 11), and the $C_m = 0.1843$ at the rearward location corresponds to a flap deflection of approximately 3.2° (green symbol in Fig. 11). The conclusion is that locating the control effector as far rearward as possible had the benefit of both the larger moment arm and the larger normal force production from the control effector.

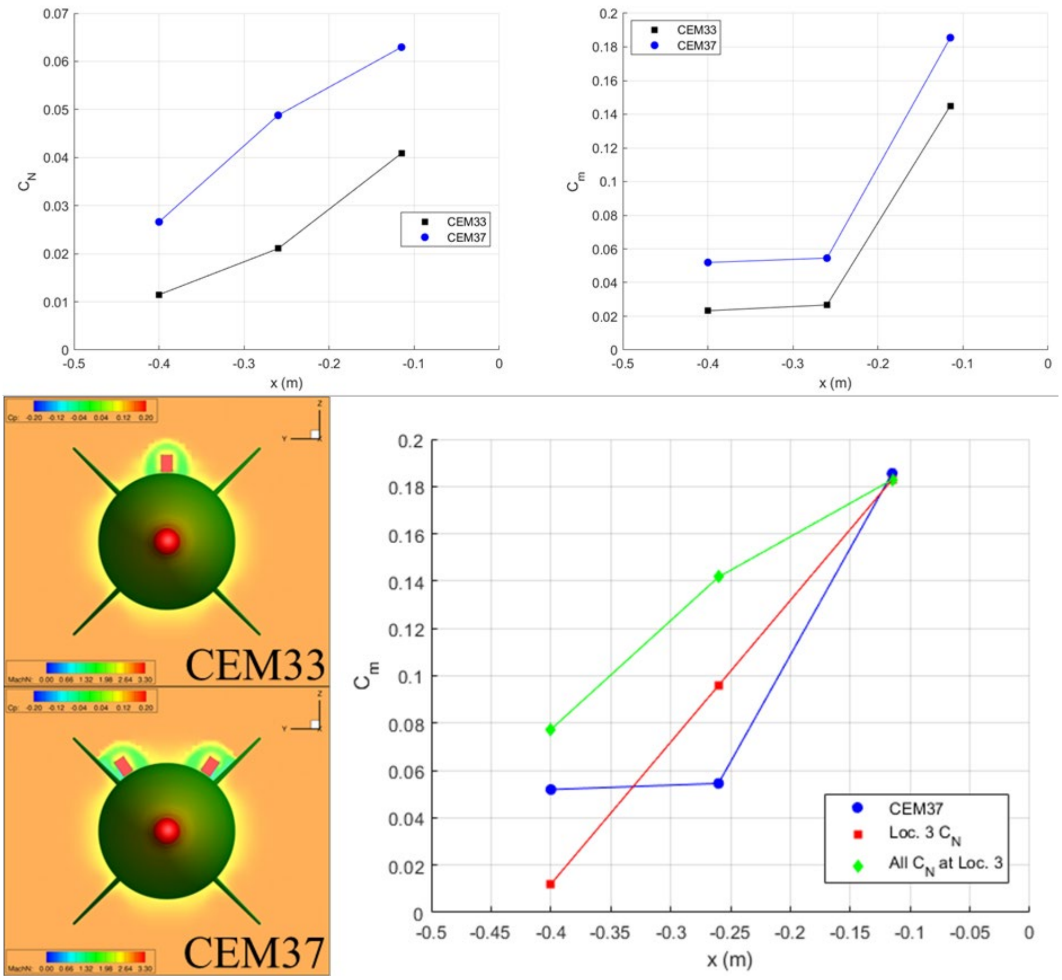

Fig. 16 C_N (top left), C_m (top right) for configurations CEM33 and CEM37 and manufactured C_m (bottom) for configuration CEM37

One comparison that can be made is to compare C_N calculated for configuration CEMX7 at the third location ($x_3 = -0.115$ m) to the C_N reported in the study by Sahu and Heavey.[10] The third location is similar to the relative placement of the micro-flaps in that study. The configuration in the study by Sahu and Heavey featured four micro-flaps compared to configuration CEMX7 in this report, which has two control effectors. Despite the configuration in the reference analyzing a different projectile with different control effector dimensions and very different vehicle configuration, the C_N calculated in each case is comparable. The magnitude of the C_N predicted by Sahu and Heavey is approximately 0.11 while the C_N calculated for configuration CEM37 at the third location is 0.063. It is also worth noting the boundary layer thickness was calculated to grow from 10.6 to 12.7 mm from -0.315 m $< x < -0.115$ m. For a pin size of 3 at the third location, over 96% of the control effector is within the boundary layer.

Figure 17 shows the results for C_l for configuration CEM310 comparing the different axial locations. The normal force and pitching moment were zero for this case. The C_l data also indicates that locating the control effector at the farthest rearward location maximizes the effectiveness of the control effector with a maximum value of almost 0.04, or equivalent flap deflection of near 3° (green symbol in left image of Fig. 13). There are apparently some nonlinear flow effects, as between stations x_1 and x_2 along the swept part of the fins (Fig. 3c)

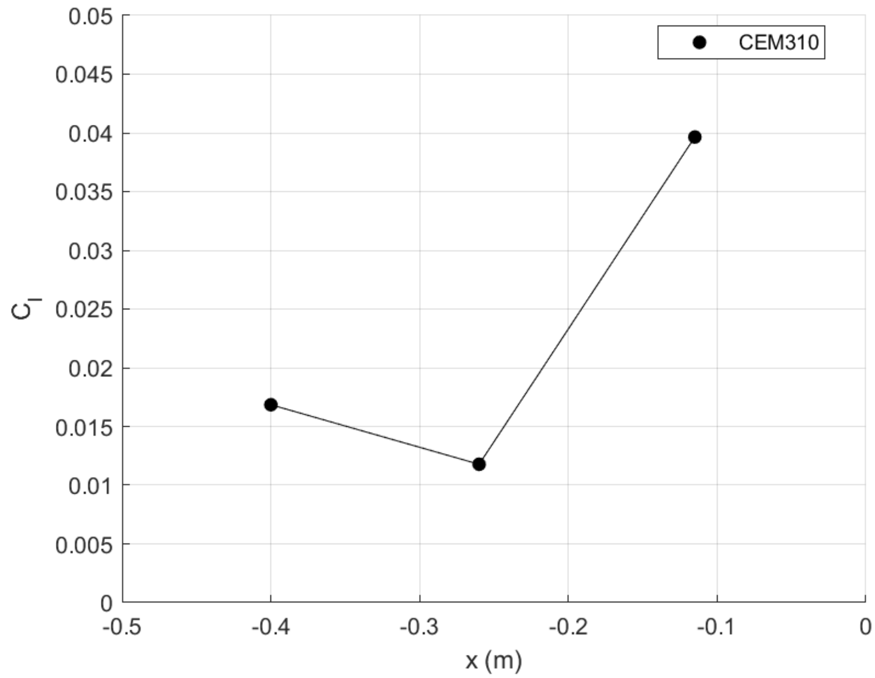

Fig. 17 C_l for configuration 10 with a pin size of 3 (CEM310)

4.4 Sweeps through Incidence Angle (α)

Two configurations were selected for analyzing the aerodynamic performance of the control effectors compared with the baseline configuration (no control effectors) at the rearward axial location. The two configurations were CEM37 and CEM310, and the range of incidence angle chosen was from $-15° \leq \alpha \leq 15°$. Figures 18 and 19 present the data for C_N as a function of α. Figures 20 and 21 present the data for C_m as a function of α. Figure 22 presents the data for C_l as a function of α. The normal force and pitching moment generated by the control effectors, ΔC_N and ΔC_m, in Figs. 19 and 21 were calculated using Eqs. 1 and 2, respectively, where "configuration" indicates the vehicle with control effectors and "baseline" indicates the vehicle with no control effectors.

$$\Delta C_N = C_{N_{configuration}} - C_{N_{baseline}} \quad (1)$$

$$\Delta C_m = C_{m_{configuration}} - C_{m_{baseline}} \qquad (2)$$

There is relatively little difference in the values of normal force generated by all three configurations on the scale used in Fig. 18. However, the differences become observable when isolating the normal force generated by the control effectors (Fig. 19). Both configurations show increasing ΔC_N as α increases and CEM310 appears shifted up from CEM37 by approximately $\Delta C_N \approx 0.065$. However, the magnitude of ΔC_N remains small for CEM310 for $-11° < \alpha < 11°$ while the magnitude of ΔC_N decreases as α increases for CEM37. For configuration CEM37, the ΔC_N is negative at zero incidence because the direction is downward. The magnitude of ΔC_N decreases with increasing incidence angle above zero because the control effectors are increasingly in the shadow of the body (leeward sides). Alternatively, the magnitude of ΔC_N increases with decreasing incidence angle below zero because the control effectors are directly in the path of the flow (windward side). For configuration CEM310, the normal force is near zero at zero incidence angle since the configuration is symmetric. There is a small increase in normal force magnitude with increasing incidence angle magnitude, which may cause some additional control requirements. However, the normal force magnitudes are fairly level, near zero for about $-10° \leq \alpha \leq 10°$, which is a reasonably large range for high-speed vehicles.

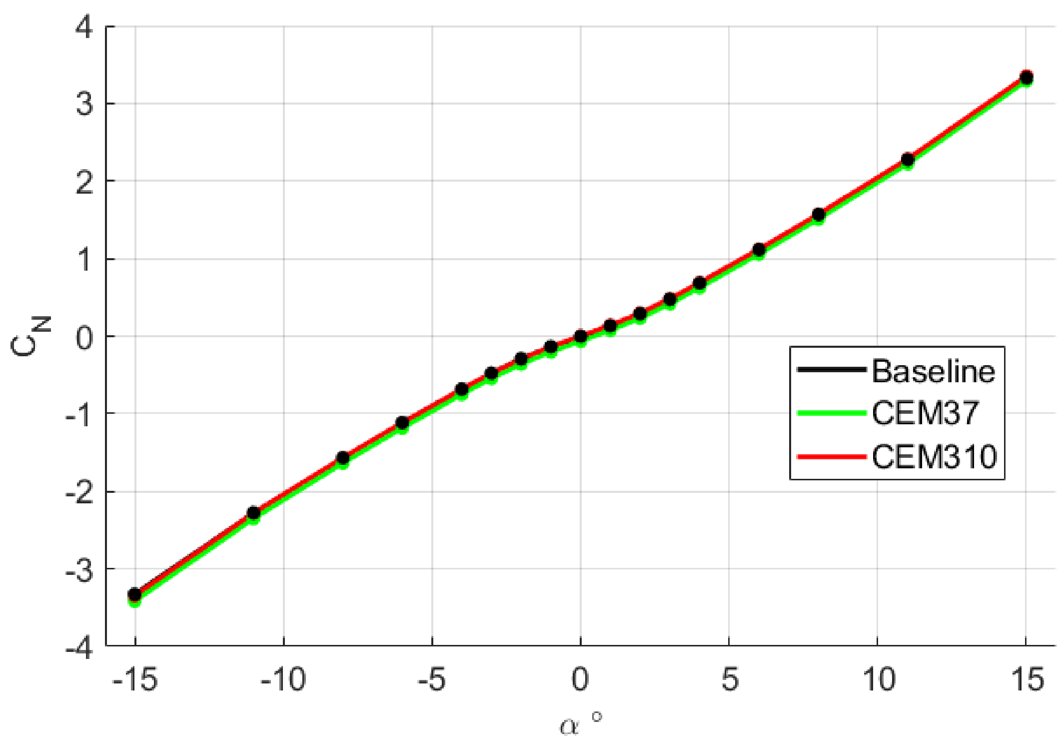

Fig. 18 C_N for the baseline configuration, CEM37, and CEM310

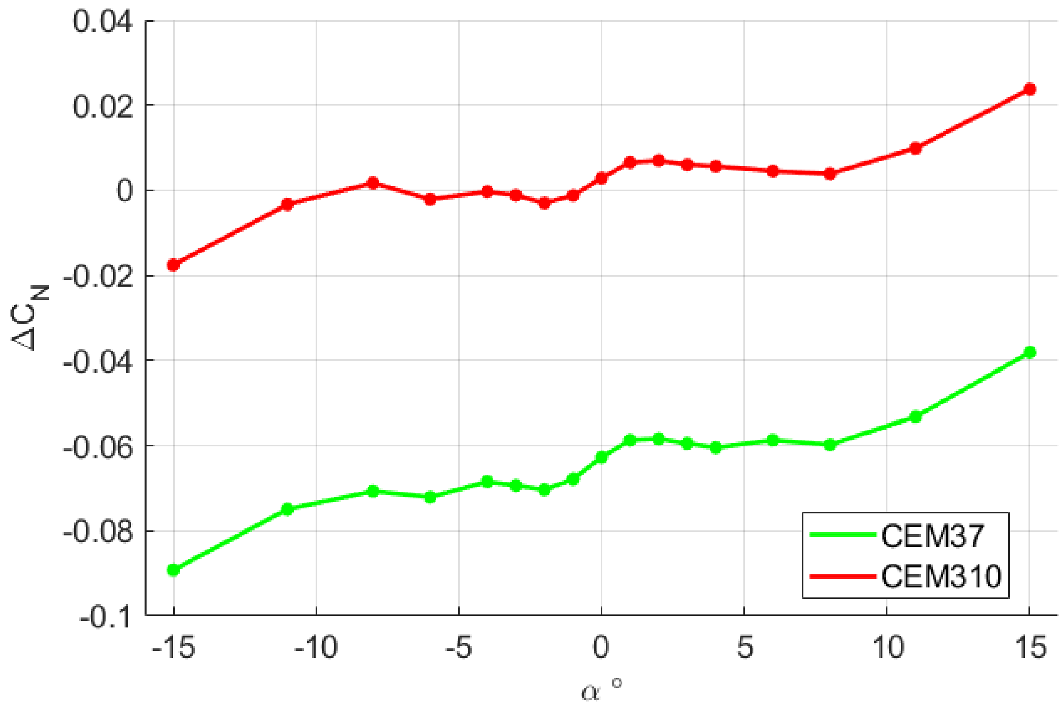

Fig. 19 ΔC_N for CEM37 and CEM310 with respect to the baseline configuration

The trend in pitching moment (Fig. 20) is a bit more difficult to analyze because the stability margin for this vehicle at this moment reference point location ($x_{c.g.}$) is very small (typical for a highly maneuverable vehicle). The baseline vehicle is unstable at small incidence angle with a trim angle of about $|\alpha| = 5°$. Configuration CEM37 (pitch control) shows the increase in C_m due to the control effector, while configuration CEM310 (roll control) shows minimal change in C_m from the baseline until $|\alpha| = 10°$ due to the effects of ΔC_N discussed in Fig. 19. The trends in ΔC_m (Fig. 21) follow the same reasoning as in the discussion of the trends in ΔC_N, that is, an increasing value of ΔC_N leads to a decreasing value of ΔC_m. The main takeaway from these trends is that for moderate incidence angles, $|\alpha| = 10°$, the roll control authority (configuration CEM310) is relatively constant while the pitch control (CEM37) is only moderately degraded by being in the shadow of the body with some added pitch control when on the windward side (negative incidence here). One might use the pitch control effectors on the windward side to more quickly return the vehicle to zero incidence after a nose-up maneuver.

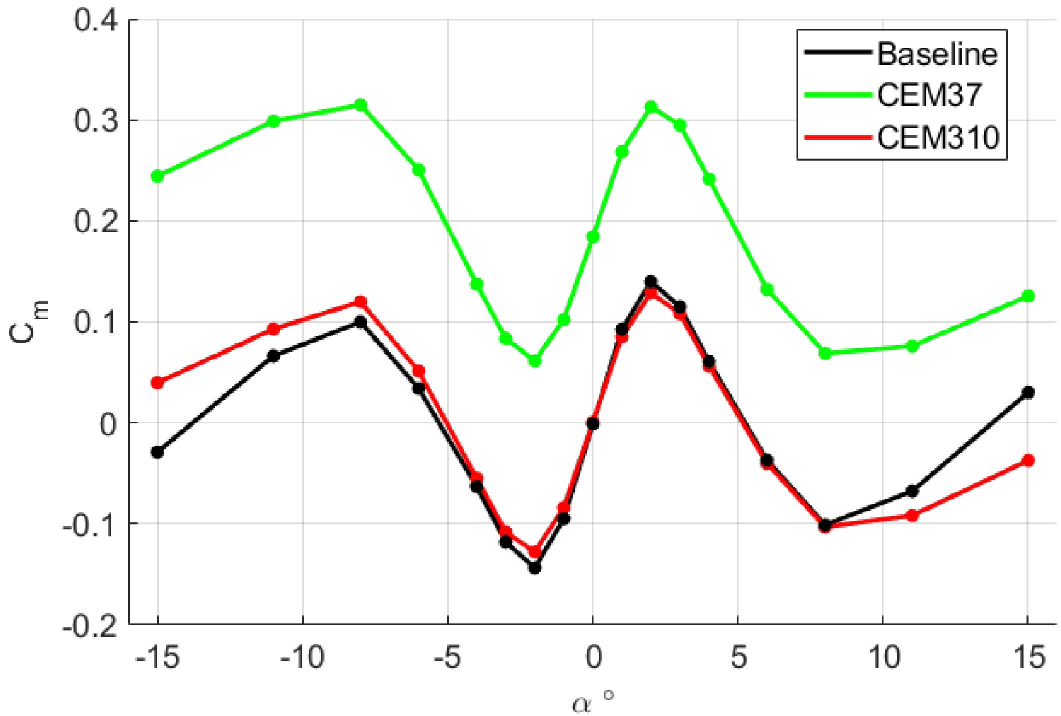

Fig. 20 C_m **for the baseline configuration, CEM37, and CEM310**

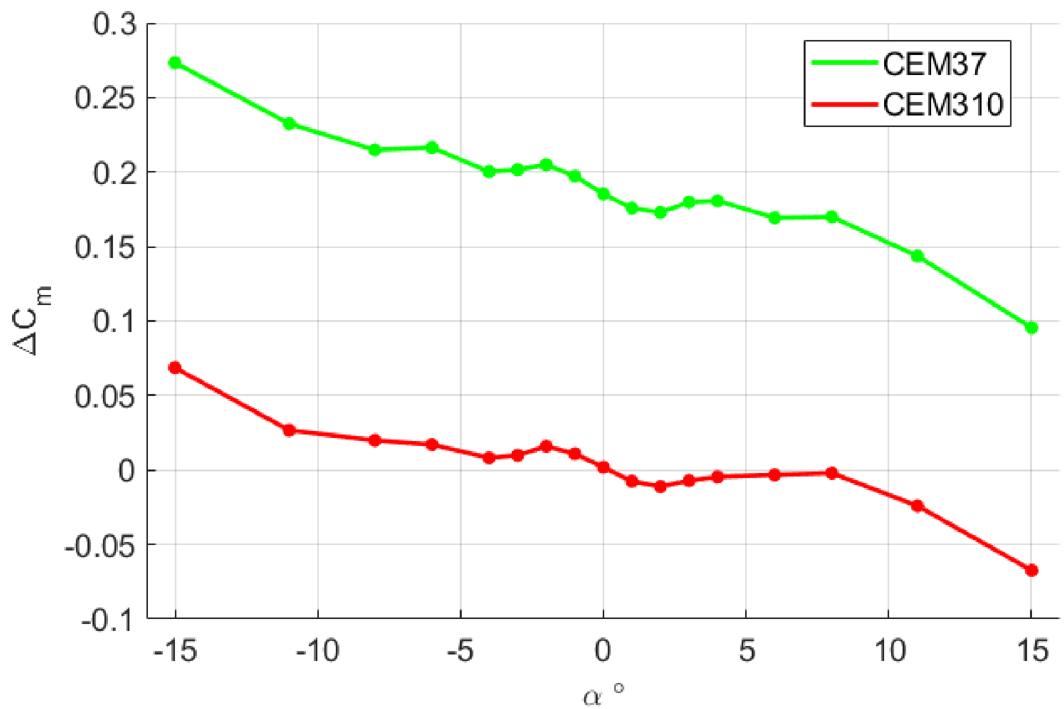

Fig. 21 ΔC_m **for CEM37 and CEM310 with respect to the baseline configuration**

The final plot in Fig. 22 shows that CEM310 is the only configuration with appreciable C_l, which is the expected result. The rolling control authority of the control effectors is shown to be highest at low to moderate α of $-8° < \alpha < 8°$, which then decreases at larger magnitudes of α. However, the diminished control authority still retains approximately 70% of performance at higher α magnitude.

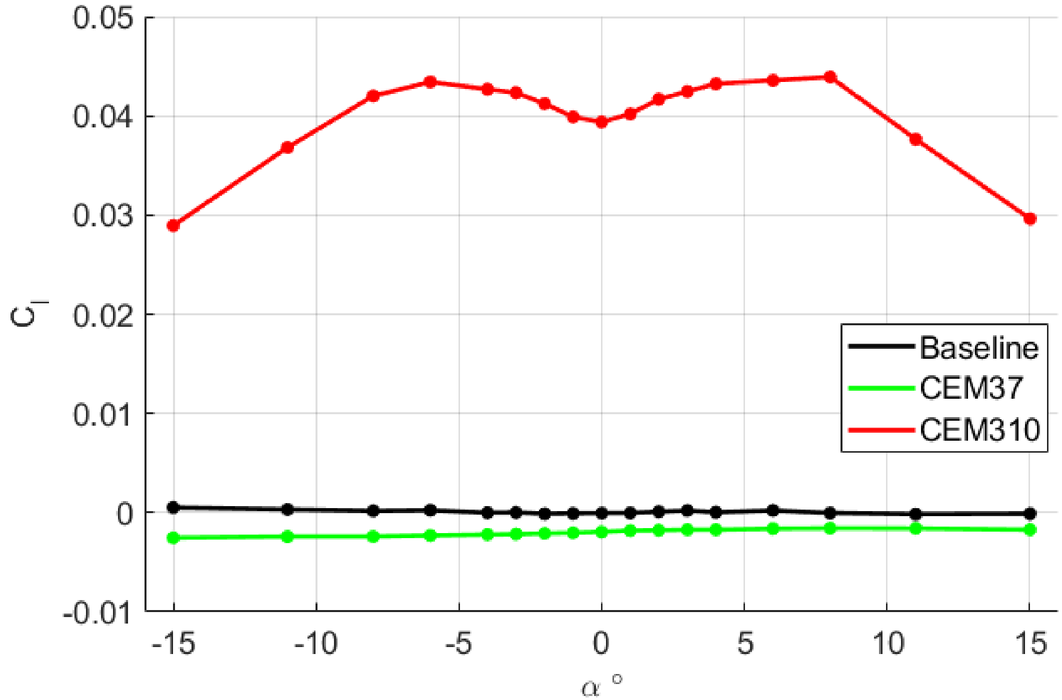

Fig. 22 C_l **for the baseline configuration, CEM37, and CEM310**

5. Conclusion

Six configurations of a generic high-speed test vehicle with control effectors were evaluated in this investigation. Three of the six configurations were selected as configurations recommended for additional investigation and analysis. Two configurations were selected for evaluating their performance across α. The effectiveness of using control effectors to accomplish pitch and roll maneuvers was demonstrated within the context of a well-established tail-flap control mechanism.

The control effectors were observed to have plausible viability, but additional analysis and potential experimentation are required to confirm this hypothesis. The analysis of different axial locations for the control effectors indicates that the third location, close to the projectile base, is the better of the three locations for using the control effector to generate a pressure distribution against the surface of the projectile and the fins. The analysis shows that the maximum C_m, C_N, and C_l are generated at the third location. The maximum moment values are not explained simply by larger moment arms.

Assessing performance as it varies with respect to α, the expected trends were observed. As α increased, ΔC_N increased while ΔC_m decreased for both configurations CEM37 and CEM310. However, the magnitudes of both ΔC_N and ΔC_m are relatively small for $-11° < \alpha < 11°$ for configuration CEM310. But the magnitudes of both ΔC_N and ΔC_m decrease with increasing α for configuration CEM37. Configuration CEM310 is the only configuration with appreciable rolling control authority.

Additional analyses are planned of variation in aerodynamic performance with Mach number, total angle of attack, and roll angle on the effectiveness of control effectors compared to tail-flap control. This includes running Navier–Stokes computations and investigating arrays of multiple pins similar to the arrays of "pin-like" control effectors previously investigated.[9–11,14,15] These additional analyses should address the validity of using Euler CFD to analyze this form of aerodynamic control. This future work can also help answer questions about interactions between control effectors in proximity and how those interactions can be leveraged to improve desired aerodynamic performance. Experiments that would further develop understanding of this technology include wind tunnel tests or free-flight experiments with control effector prototypes in different configurations for both pitch and roll maneuvers on a generic high-speed projectile.

6. References

1. Massey CK, Guthrie BK. Optimized guidance of a supersonic projectile using pin based actuators. 23rd AIAA Applied Aerodynamics Conference; 2005 June. AIAA 2005-4966.

2. Massey CK, McMichael J, Warnock T, Hay F. Mechanical actuators for guidance of a supersonic projectile. 23rd AIAA Applied Aerodynamics Conference; 2005 June. AIAA 2005-4970.

3. Massey CK, Silton IS. Testing the maneuvering performance of a Mach 4 projectile. 24th Applied Aerodynamics Conference; 2006 June. AIAA 2006-3649.

4. Silton IS, Massey CK. Investigation of actuator performance for guiding supersonic projectiles. J Spacecr Rockets. 2008 May–June;45(3).

5. Massey CK, McMichael J, Warnock T, Hay F. Mechanical actuators for guidance of a supersonic projectile. J Spacecr Rockets. 2008 July–Aug;45(4).

6. Massey CK, Silton IS. Combining experimental data, computational fluid dynamics, and six-degree of freedom simulation to develop a guidance actuator for a supersonic projectile. J Aerosp Eng. 2008 Nov;223(Part G).

7. Celmins I. Design and evaluation of an electromechanical actuator for projectile guidance. Army Research Laboratory (US); 2007 Sep. Report No.: ARL-MR-0672.

8. Bell M, Watterson KJ, Lisk D. A numerical study into a local protuberance interaction with a fin on a supersonic projectile. 47th AIAA Aerospace Sciences Meeting; 2009 Jan. AIAA 2009-1092.

9. Dykes J, Montalvo C, Costello M, Sahu J. Use of microspoilers for control of finned projectiles. J Spacecr Rockets. 2012 Nov–Dec;49(6).

10. Sahu J, Heavey RK. Parallel CFD computations of projectile aerodynamics with a flow control mechanism. Comput Fluids. 2013;88.

11. Scheuermann E, Costello M, Silton S, Sahu J. Aerodynamic characterization of a microspoiler system for supersonic finned projectiles. J Spacecr Rockets. 2015 Jan–Feb;52(1).

12. Fresconi F, Guidos B, Celmins I, Hathaway W. Flight behavior of an asymmetric body through spark range experiments using roll-yaw resonance for yaw enhancement. AIAA SciTech; 2016 Jan. AIAA 2016-0782.

13. Fresconi F, Guidos B, Celmins I, Hathaway W. Flight behavior of an asymmetric missile through advanced characterization techniques. J Spacecr Rockets. 2017 Jan–Feb;54(1).

14. Dooroo K, Strickland L, Gross M, Rogers J, Costello M, Fresconi F, Celmins I. Actuator design and flight testing of an active microspoiler-equipped projectile. Journal of Dynamic Systems Measurement and Control. 2017 Nov;139:111002.

15. Leonard A, Rogers J, Sahu J. Aerodynamic optimization of microspoiler actuators for guided projectiles. J Spacecr Rockets. 2017 Nov–Dec;54(6).

16. Bryson JT, Vasile JD, Gruenwald BC, Sahu J, Fresconi F. Modeling and flight dynamics of a projectile with nonlinear, roll-dependent aerodynamics. AIAA SciTech Forum; 2021 Jan. AIAA-2021-0823. doi: 10.2514/6.2021-0823

17. Vasile JD, Bryson JT, Gruenwald BC, Fairfax LD, Strohm LS, Fresconi F. A multi-disciplinary approach to design long range guided projectiles. 2020 AIAA Science and Technology Forum; 2020 Jan. AIAA-2020-1993.

18. Vasile JD, Bryson JT, Fresconi F. Aerodynamic design optimization of long-range projectiles using missile DATCOM. 2020 AIAA Science and Technology Forum; 2020 Jan. AIAA-2020-1762.

19. Paul JL, Vasile JD, DeSpirito J. Comparison of aeroprediction methods for guided munitions. DEVCOM Army Research Laboratory (US); 2021 Sep. Report No.: ARL-TR-9287

20. Burchett BT, Paul JL, Vasile JD, Bryson JT. A high-fidelity, roll-dependent aerodynamic model for a long-range, high-speed missile. DEVCOM Army Research Laboratory (US); 2021 July. Report No.: ARL-TR-9236.

21. Vasile JD, Sahu J. Roll orientation-dependent aerodynamics of a long-range projectile. DEVCOM Army Research Laboratory (US); 2020 Aug. Report No.: ARL-TR-9017.

22. Vasile JD, Bryson JT, Sahu J, Paul JL. Aerodynamic dataset generation of a long-range projectile. DEVCOM Army Research Laboratory (US); 2020 Aug. Report No.: ARL-TR-9019.

23. Pokela R, Kumar R, Vasile JD, DeSpirito J. Aerodynamic characterization of a generic high-speed projectile configuration. J Spacecr Rockets. 2024 Jan–Feb;61(3).

24. Bryson J, Vasile J, Gruenwald B, Fresconi F. Control surface design analysis and actuation requirements development for munitions. AIAA SciTech 2020 Forum; 2020 Jan. AIAA-2020-0020.

25. Aftosmis MJ, Berger MJ, Adomavicius G. A parallel multilevel method for adaptively refined Cartesian grids with embedded boundaries. 38th Aerospace Sciences Meeting and Exhibit; 2000 Jan. AIAA-2000-0808.

26. Nemec M, Aftosmis MJ, Wintzer M. Adjoint-based adaptive mesh refinement for complex geometries. 46th AIAA Aerospace Sciences Meeting; 2008 Jan. AIAA-2008-0725.

27. Berger MJ, Aftosmis MJ, Marshal DD, Murman SM. Performance of a new CFD flow solver using a hybrid programming paradigm. J Para Dist Comp. 2004.

Appendix. Tabulated Data

Table A-1 Tabulated data of control effector configurations at Mach 3 and $\alpha = 0°$

Configuration	C_N	C_m	C_l
CEM13	–0.0047	0.0167	–0.0001
CEM23	–0.0563	0.1986	0.0000
CEM33	–0.0408	0.1448	0.0000
CEM16	–0.0041	0.0123	0.0014
CEM26	–0.0405	0.1260	0.0112
CEM36	–0.0292	0.0900	0.0084
CEM17	–0.0085	0.0250	–0.0002
CEM27	–0.0885	0.2615	–0.0032
CEM37	–0.0628	0.1843	–0.0019
CEM28	–0.1064	0.2820	–0.0034
CEM38	–0.0748	0.1985	–0.0020
CEM110	0.0004	–0.0004	0.0063
CEM210	0.0049	–0.0008	0.0543
CEM310	0.0029	0.0009	0.0394
CEM111	0.0004	–0.0004	0.0030
CEM211	0.0050	–0.0010	0.0255
CEM311	0.0030	0.0004	0.0187

Table A-2 Tabulated data of control effector configurations at Mach 3 and $\alpha = 0°$ at different axial locations

$x_1 = –0.400$ m

Configuration	C_N	C_m
CEM33	0.0115	0.0233
CEM37	–0.0260	–0.0537

$x_2 = –0.260$ m

Configuration	C_N	C_m
CEM33	0.0211	0.0267
CEM37	–0.0486	0.0535

$x_3 = –0.115$ m

Configuration	C_N	C_m
CEM33	–0.0408	0.1448
CEM37	–0.0628	0.1843

Table A-3 Tabulated data of baseline configuration at Mach 3

$\alpha°$	C_N	C_m	C_l
–15	–3.3272	–0.0290	0.0005
–11	–2.2746	0.0663	0.0003
–8	–1.5667	0.1001	0.0002
–6	–1.1142	0.0341	0.0002
–4	–0.6831	–0.0630	0.0000
–3	–0.4761	–0.1179	0.0000
–2	–0.2881	–0.1434	–0.0001
–1	–0.1341	–0.0948	–0.0001
0	0.0000	–0.0010	–0.0001
1	0.1346	0.0927	0.0000
2	0.2900	0.1400	0.0001
3	0.4770	0.1150	0.0002
4	0.6840	0.0608	0.0000
6	1.1155	–0.0368	0.0002
8	1.5672	–0.1009	0.0000
11	2.2750	–0.0675	–0.0002
15	3.3279	0.0303	–0.0001

Table A-4 Tabulated data of configuration CEM37 at Mach 3

$\alpha°$	C_N	C_m	C_l
–15	–3.4164	0.2443	–0.0025
–11	–2.3495	0.2988	–0.0024
–8	–1.6374	0.3148	–0.0024
–6	–1.1863	0.2505	–0.0023
–4	–0.7515	0.1373	–0.0022
–3	–0.5455	0.0837	–0.0022
–2	–0.3584	0.0615	–0.0021
–1	–0.2020	0.1025	–0.0020
0	–0.0628	0.1843	–0.0019
1	0.0759	0.2685	–0.0018
2	0.2316	0.3129	–0.0018
3	0.4175	0.2948	–0.0017
4	0.6236	0.2415	–0.0017
6	1.0568	0.1325	–0.0016
8	1.5074	0.0690	–0.0016
11	2.2218	0.0761	–0.0016
15	3.2898	0.1257	–0.0017

Table A-5 Tabulated data of configuration CEM310 at Mach 3

$\alpha°$	C_N	C_m	C_l
–15	–3.3447	0.0397	0.0289
–11	–2.2779	0.0930	0.0368
–8	–1.5650	0.1200	0.0420
–6	–1.1163	0.0512	0.0434
–4	–0.6834	–0.0548	0.0427
–3	–0.4773	–0.1080	0.0423
–2	–0.2911	–0.1275	0.0412
–1	–0.1353	–0.0838	0.0399
0	0.0029	0.0009	0.0394
1	0.1412	0.0853	0.0402
2	0.2970	0.1290	0.0417
3	0.4830	0.1080	0.0425
4	0.6897	0.0563	0.0432
6	1.1200	–0.0400	0.0436
8	1.5711	–0.1029	0.0439
11	2.2849	–0.0915	0.0376
15	3.3517	–0.0371	0.0296

List of Symbols, Abbreviations, and Acronyms

CFD computational fluid dynamics

NASA National Aeronautics and Space Administration

Nomenclature

α = angle of attack, °

δ = flap deflection angle, °

C_l = rolling moment coefficient

C_m = pitching moment coefficient

C_N = normal force coefficient

C_p = pressure coefficient

M = Mach number

x = distance along vehicle axis referenced from base, m

$x_{c.g.}$ = axial location of vehicle center of gravity referenced from base, m

y = lateral distance referenced from vehicle axis, m

z = longitudinal distance referenced from vehicle axis, m

1 (PDF)	DEFENSE TECHNICAL INFORMATION CTR DTIC OCA
1 (PDF)	DEVCOM ARL FCDD RLB CI TECH LIB